An Approach to Suppress Low Frequency Oscillation in the Traction Network of High-Speed Railway Using Passivity-Based Control

Zhigang Liu, *Senior Member, IEEE*, Zhaozhao Geng, and Xinxuan Hu

***Abstract*—The traction blockade in depots of multiple electric multiple units (EMUs) is generally considered to be caused by the voltage low frequency oscillation (LFO) of the high-speed railway traction network. As a possible solution, a strategy using single-phase EMUs rectifiers with passivity-based control (PBC) is proposed in this paper. First, the mathematical model of the four-quadrant pulse width modulation rectifier is constructed based on the port controlled Hamiltonian with dissipation. Next, with the insertion of damping, the new energy function can be minimized at the equilibrium point of the system, which enables the derivation of the rectifier control law based on the interconnection and damping assignments PBC. Comparison of simulation results with those of the traditional proportional integral (PI) scheme, autodisturbance rejection control and multivariable control verifies that the proposed PBC controller has better dynamic and static performance. Among all strategies considered, the resulting line current has the least total harmonic distortion, and the dc-link voltage of single-phase EMUs rectifier has the least oscillation and the shortest adjustment time, when using the PBC. Meanwhile, the simulations of multi-EMUs accessed a traction network show that the proposed method significantly suppresses the voltage LFO of the traction network. Finally, the LFO signal modal analysis is performed using the fast Fourier transform and the estimating signal parameters via the rotational invariance techniques. It indicates that PBC can suppress the symmetrical frequency components and effectively reduce the third, fifth, and other harmonic components compared with the PI control in EMUs.**

***Index Terms*—High-speed railway, EMUs-traction network, low frequency oscillation, pulse rectifier, PBC controller.**

NOMENCLATURE

EMUs	Electric multiple units.
LFO	Low frequency oscillation.
PI	Proportional integral.
ETNCS	EMUs-traction network cascade system.
MC	Multivariable control.
ADRC	Auto-disturbance rejection control.
PBC	Passivity-based control.
IDA-PBC	Interconnection and damping assignment passivity-based control.
PCHD	Port controlled Hamiltonian with dissipation.
PWM	Pulse width modulation.
GSSA	Generalized state space averaging.
FFT	Fast Fourier transform.
THD	Total harmonic distortion.
ESPRIT	Estimating signal parameters via the rotational invariance techniques.

Manuscript received March 6, 2017; revised August 8, 2017 and October 29, 2017; accepted January 1, 2018. Date of publication January 4, 2018; date of current version June 18, 2018. This work was supported in part by the National Nature Science Foundation of China under Grant U1434203 and Grant U1734202, and in part by the Sichuan Province Youth Science and Technology Innovation Team Funding in China under Grant 2016TD0012. Paper no. TPWRS-00324-2017. *(Corresponding author: Zhigang Liu.)*

The authors are with the School of Electrical Engineering, Southwest Jiaotong University, Chengdu 610031, China (e-mail: liuzg_cd@126.com; 939066877@qq.com; 714352246@qq.com).

Color versions of one or more of the figures in this paper are available online at http://ieeexplore.ieee.org.

Digital Object Identifier 10.1109/TPWRS.2018.2789450

I. INTRODUCTION

WITH the rapid development of high-speed railways in recent years, large quantities of AC-DC-AC drive electric multiple units (EMUs) and electric locomotives have been put into operation. Due to the heavy operation of EMUs and electric locomotives, some voltage low frequency oscillation (LFO) events have occurred worldwide when multiple vehicles were connected to the grid [1]. The LFOs resulted in traction blockade accidents, which obstructed the normal operation of high-speed railways [2].

Through a data analysis of these traction blockade accidents, the voltage LFO of traction network was discovered. In [2], the stability analysis of the control system using a cascade harmonic transfer function indicated that the control of the rectifier was an important factor for the stability of the vehicle-grid system. In [3], the PWM converter control system is improved and optimized, but the impact of load disturbance on the dynamic performance is not taken into account. A single-phase *dq*-decomposition method was adopted for the EMUs control, and the impact of the control parameters on the stability of the vehicle-grid system was demonstrated in [4]. Menth *et al.* noted that the number of locomotives in simultaneous operation and the control parameters would cause the LFO [5]. In [6], the influence of proportional integral (PI) parameters on the stability of the vehicle-grid system was analyzed using Hurwitz criterion and the small gain principle. The stability of an EMUs-traction network cascade system (ETNCS) was analyzed, and the quantitative indicators of the system impedance matching were given in [7]. The PI controller is simple to implement, and can make the ETNCS have the good stability, but the dynamic performance of the system deteriorates. In [8], a multivariable

control (MC) method for converters was proposed to improve the anti-oscillation quality for voltage, but the simulation results showed that the voltage waveforms of EMUs had an unstable trend because the MC still used a PI controller. The MC is a nonlinear control method based on state feedback linearization. And it transforms the original nonlinear system into a linear system characterized by the selected state variables, which is convenient for the design and implementation of the controller.

In summary, it is generally concluded that LFO is influenced by the control of the EMUs rectifiers. At present, the traditional linear PI controller is most commonly used. However, the PI regulator has a complex structure due to the inherent double closed-loop control [9], which slows the single-phase EMUs rectifier dynamic response. In addition, it is difficult to adjust the parameters to ensure the system stability when the system is disturbed. For nonlinear EMUs rectifiers, the linearization is not suitable when the rectifier is required to function over a wide operating range. To prevent these issues, several nonlinear methods have been proposed [10]–[14]. In [10], [11], a nonlinear auto-disturbance rejection control (ADRC) method for converters was proposed to achieve a better suppression of the oscillation voltage. The ADRC controller is a nonlinear controller for an uncertain system. The core advantage of ADRC includes that the state variables of the system can be observed by expanding the observer, observing the comprehensive disturbance of the system, obtaining the compensating the disturbance. But it requires setting many parameters. A passivity-based control (PBC) of the elastic joint robot was proposed in [12], which demonstrated good performance regarding both vibration suppression and tracking precision of the elastic joint robot control system. In [13], by the series/parallel damping of single-phase PWM voltage source converters, the PBC was put forth. For the series damping injection scheme, the addition of damping injection filters resulted in a reduction of the selected current harmonics. In [14], a novel approach for the assessment of transient stability was proposed, which generalized the idea of energy methods.

Among these nonlinear control schemes, as an important framework for the control of nonlinear systems [13], [15]–[18], PBC has paid attention in the last decade. Its design procedures include the Euler–Lagrange [17] and the interconnection and damping assignments [18]. The main advantage of PBC is the explicit use of the knowledge of the physical system structure in the controller, e.g., the energy, dissipation, and interconnections of the system. Therefore, the basic idea behind a PBC design is to modify the energy of the system and to add damping by modification of the dissipation structure [13], [15]. In this paper, the interconnection and damping assignment passivity-based control (IDA-PBC) is proposed to suppress the voltage LFO of the high-speed railway traction network.

II. Mathematical Modeling of the Single-Phase EMUs Rectifier Based on PCHD

Currently, most researchers hold the view that the cause of voltage LFO is the mismatch between the electrical parameters of the traction network and the control parameters of the line-side converters, and they propose to change the control strategy of the single-phase EMUs rectifier to suppress the phenomenon [1], [5]. To analyze the control of the single-phase EMUs rectifier, a mathematical model based on the port controlled Hamiltonian with dissipation (PCHD) is built in this paper.

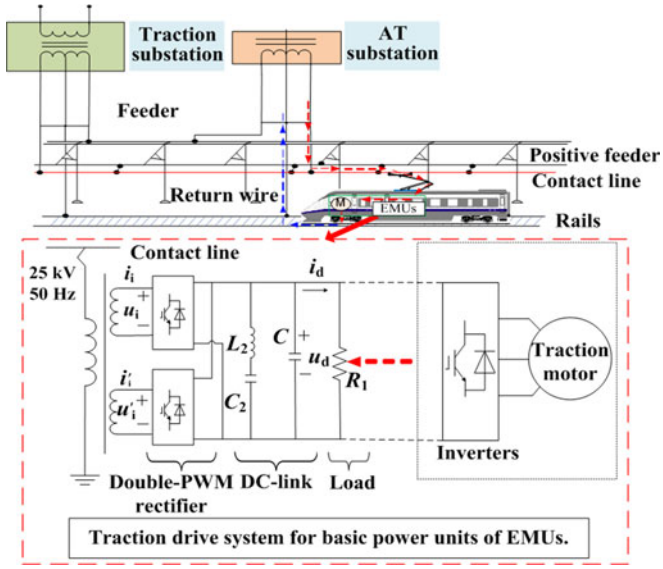

Fig. 1. Schematic of a high-speed railway ETNCS.

A. High-Speed Railway EMUs-Traction Network Cascade System

A high-speed ETNECS is composed of a traction power supply system and an EMUs' traction drive system, as shown in Fig. 1. When the nonlinear circuits of EMUs are attached to the traction network, there will be a large amount of switching ripples in the inductive current, which will increase the disturbance to the traction network and lead to the oscillation of the related voltage and current of the EMUs. In addition, the unstable output voltage and current are introduced into the closed-loop control circuit, which will lead to the distortion of the input voltage and current. With an increasing number of EMUs in operation, the distortion will be exacerbated, which leads directly to the traction blockade.

B. Mathematical Model of the Single-Phase EMUs Rectifier Based on PCHD

The transmission system of an EMUs basic power unit is shown in Fig. 1. The rectifier part of the traction drive system of the EMUs includes a double-four quadrant pulse width modulation (PWM) rectifier. When the traction blockade occurs, a large number of EMUs are at a standstill with only the auxiliary load powered by the DC-link of the traction converters. Therefore, some simplifications can be made for the inverter and traction motor of the EMUs' traction driver system [9]. In addition, the topologies of each rectifier unit of the double-four quadrant rectifier are the same. Hence, the single four-quadrant rectifier equivalent circuit can be established, as shown in Fig. 2.

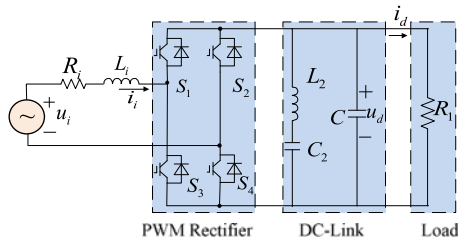

Fig. 2. Equivalent circuit of single four-quadrant pulse rectifier.

In Fig. 2, $u_i = u_i(t) = U_{im}\sin(\omega_s t)$ represents the line voltage, where U_{im} is the voltage amplitude, and i_i represents the line current. L_i and R_i are the equivalent inductance and resistance of the secondary winding of the traction transformer, respectively. The second-order filter circuit is composed of L_2 and C_2. $u_d = u(t)$,i_d, C and R_1 denote the DC-link voltage, current, capacitance and equivalent load, respectively. The switching states are given by S_1, S_2, S_3 and S_4.

Assuming that each power switch is an ideal device, the switching function can be defined as

$$S = \begin{cases} 1 & (S_1, S_4 \text{ are closed}; \quad S_2, S_3 \text{ are open}) \\ -1 & (S_1, S_4 \text{ are open}; \quad S_2, S_3 \text{ are closed}) \end{cases} \tag{1}$$

The magnetic flux $\phi(t)$ goes through inductor L_i and the electrical charge $q(t)$ in capacitor C is used as the state variable, and the state space model of the system is established according to Fig. 2. The second-order filter circuit composed of L_2 and C_2 is not considered, since it almost has no effect on the establishment of the state space model (2) [9].

$$\begin{cases} \dfrac{d\phi(t)}{dt} = -\dfrac{S}{C}q(t) - \dfrac{R_i}{L_i}\phi(t) + u_i \\ q(t)\dfrac{dq(t)}{dt} = \dfrac{S}{L_i}\phi(t)q(t) - i_d q(t) \end{cases} \tag{2}$$

To simplify the study, new variables are introduced as

$$z_1(t) = \phi(t), \quad z_2(t) = \frac{1}{2}q(t)^2 \quad \text{and} \quad \upsilon(t) = -Sq(t).$$

Substituting these new variables into (2), it follows that

$$\begin{cases} \dfrac{dz_1(t)}{dt} = -\dfrac{R_i z_1(t)}{L_i} + \dfrac{\upsilon(t)}{C} + u_i \\ \dfrac{dz_2(t)}{dt} = -\dfrac{\upsilon(t)z_1(t)}{L_i} - i_d(t)\sqrt{2z_2(t)} \end{cases} \tag{3}$$

According to the expected dynamic characteristics of variables $z_1(t)$, $z_2(t)$ and $\upsilon(t)$, the generalized state space averaging (GSSA) model of the single-phase EMUs PWM rectifier should consider the fundamental Fourier term of $z_1(t)$, the constant term of $z_2(t)$ and the fundamental Fourier term of $\upsilon(t)$ [19]. The variable $z_1(t)$ can be represented by the Fourier series as follows.

$$\begin{aligned} z_1(t) &= \langle z_1(t)\rangle_0 + 2\sum_k^{\infty}\left(\langle z_1(t)\rangle_k^R \cos(\omega t) - \langle z_1(t)\rangle_k^I \sin(\omega t)\right) \\ &\approx 2\left(\langle z_1(t)\rangle_1^R \cos(\omega t) - \langle z_1(t)\rangle_1^I \sin(\omega t)\right) \end{aligned} \tag{4}$$

Similarly, it follows that

$$\begin{aligned} z_2(t) &\approx \langle z_2(t)\rangle_0 \\ \upsilon(t) &\approx 2\left(\langle \upsilon(t)\rangle_1^R \cos(\omega t) - \langle \upsilon(t)\rangle_1^I \sin(\omega t)\right) \end{aligned} \tag{5}$$

where $\langle z_1(t)\rangle_1^R$ and $\langle z_1(t)\rangle_1^I$ are the real and imaginary parts of the $z_1(t)$ fundamental Fourier term, respectively. $\langle z_2(t)\rangle_0$ denotes the constant term of $z_2(t)$. $\langle \upsilon(t)\rangle_1^R$ and $\langle \upsilon(t)\rangle_1^I$ represent the real and imaginary parts of the $\upsilon(t)$ fundamental Fourier term, respectively.

Considering the relevant Fourier components and using (4), the bilinear product $\upsilon(t)z_1(t)$ in (3) can be approximated as

$$\langle \upsilon(t)z_1(t)\rangle_0 \approx 2\left(\langle \upsilon(t)\rangle_1^R \langle z_1(t)\rangle_1^R + \langle \upsilon(t)\rangle_1^I \langle z_1(t)\rangle_1^I\right) \tag{6}$$

Furthermore,

$$\langle i_d q(t)\rangle_0 = \langle i_d\rangle_0\langle q(t)\rangle_0 + 2(\langle i_d\rangle_1^R \langle q(t)\rangle_1^R + \langle i_d\rangle_1^I \langle q(t)\rangle_1^I \tag{7}$$

The state vector $\boldsymbol{x}$ and control vector $\boldsymbol{u}$ are defined as follows.

$$\begin{aligned} [x_1, x_2, x_3]^T &= \left[\langle z_2(t)\rangle_0, \langle z_1(t)\rangle_1^R, \langle z_1(t)\rangle_1^I\right]^T \\ [u_1, u_2]^T &= \left[\langle \upsilon(t)\rangle_1^R, \langle \upsilon(t)\rangle_1^I\right]^T \end{aligned} \tag{8}$$

From (4)–(7), the GSSA mathematical model of the single-phase EMUs rectifier can be derived as

$$\begin{cases} \dot{x}_1 = -i_d\sqrt{2x_1} - \dfrac{2}{L_i}u_1 x_2 - \dfrac{2}{L_i}u_2 x_3 \\ \dot{x}_2 = -\dfrac{R_i}{L_i}x_2 + \omega_s x_3 + \dfrac{1}{C}u_1 \\ \dot{x}_3 = -\omega_s x_2 - \dfrac{R_i}{L_i}x_3 - \dfrac{U_{im}}{2} + \dfrac{1}{C}u_2 \end{cases} \tag{9}$$

Let the total energy function of the single-phase EMUs rectifier be

$$H(x) = \frac{1}{C}x_1 + \frac{1}{L_i}x_2^2 + \frac{1}{L_i}x_3^2 \tag{10}$$

The PCHD mathematical model of the single-phase EMUs rectifier is obtained as

$$\begin{aligned} \dot{\boldsymbol{x}} &= \left(\begin{bmatrix} 0 & -u_1 & -u_2 \\ u_1 & 0 & \dfrac{\omega_s L_i}{2} \\ u_2 & -\dfrac{\omega_s L_i}{2} & 0 \end{bmatrix} - \begin{bmatrix} 0 & 0 & 0 \\ 0 & \dfrac{R_i}{2} & 0 \\ 0 & 0 & \dfrac{R_i}{2} \end{bmatrix}\right) \\ &\quad \times \begin{pmatrix} \dfrac{1}{C} \\ \dfrac{2}{L_i}x_2 \\ \dfrac{2}{L_i}x_3 \end{pmatrix} + \begin{bmatrix} -\sqrt{2x_1} \\ 0 \\ 0 \end{bmatrix} i_d + \begin{bmatrix} 0 \\ 0 \\ -\dfrac{1}{2} \end{bmatrix} U_{im} \\ &= (\boldsymbol{J}(\boldsymbol{u}) - \boldsymbol{R})(\nabla H)^T + \boldsymbol{g}_1(x_1)i_d + \boldsymbol{g}_2 U_{im} \end{aligned} \tag{11}$$

where $\boldsymbol{J}(\boldsymbol{u}) = -\boldsymbol{J}^T(\boldsymbol{u}) = \boldsymbol{J}$ and $\boldsymbol{R} = \boldsymbol{R}^T \geq 0$. $\boldsymbol{J}$ and $\boldsymbol{R}$ are the interconnection structure and damping of the single-phase EMUs rectifier, respectively. $\boldsymbol{g}$ represents the port characteristic matrix of the single-phase EMUs rectifier.

The passivity is a special case of the dissipation. To accurately define the dissipation of the single-phase EMUs rectifier system, two functions are introduced, namely, the supply rate $\boldsymbol{W}$ function that reflects the rate of energy flowing into the single-phase EMUs rectifier, and the non-negative storage function that measures the energy stored in the single-phase EMUs rectifier. If the single-phase EMUs rectifier is dissipated, the external energy supplied to the single-phase EMUs rectifier should not be less than the increased energy in the single-phase EMUs rectifier over a given period of time.

The total energy function of the single-phase EMUs rectifier is taken as its storage function

$$H(\boldsymbol{x}) = \frac{1}{C}x_1 + \frac{1}{L_i}x_2^2 + \frac{1}{L_i}x_3^2 \tag{12}$$

Then

$$\begin{aligned}\frac{dH(\boldsymbol{x})}{dt} &= \left(\frac{\partial H(\boldsymbol{x})}{\partial \boldsymbol{x}}\right)\dot{\boldsymbol{x}} = \left(\frac{\partial H(\boldsymbol{x})}{\partial \boldsymbol{x}}\right) \\ &\quad \times \left[(\boldsymbol{J}(\boldsymbol{u}) - \boldsymbol{R})(\nabla H)^T + \boldsymbol{g}_1(x_1)i_d + \boldsymbol{g}_2 U_{im}\right] \\ &= -\frac{\partial H(\boldsymbol{x})}{\partial \boldsymbol{x}}\boldsymbol{R}(\boldsymbol{x})\left(\frac{\partial H(\boldsymbol{x})}{\partial \boldsymbol{x}}\right)^T + \boldsymbol{W} + \frac{\partial H(\boldsymbol{x})}{\partial \boldsymbol{x}}\boldsymbol{g}_1(x_1)i_d\end{aligned} \tag{13}$$

Taking $\boldsymbol{Q}(\boldsymbol{x}) = \frac{\partial H(\boldsymbol{x})}{\partial \boldsymbol{x}}\boldsymbol{R}(\boldsymbol{x})(\frac{\partial H(\boldsymbol{x})}{\partial \boldsymbol{x}})^T > 0$ as a positive definite function, and $\frac{\partial H(\boldsymbol{x})}{\partial \boldsymbol{x}}\boldsymbol{g}_1(x_1)i_d < 0$, it follows that

$$\frac{dH(\boldsymbol{x})}{dt} = \boldsymbol{W} - \boldsymbol{Q}(\boldsymbol{x}) + \frac{\partial H(\boldsymbol{x})}{\partial \boldsymbol{x}}\boldsymbol{g}_1(x_1)i_d \leq \boldsymbol{W} - \boldsymbol{Q}(\boldsymbol{x}) \tag{14}$$

Equation (14) shows that the external energy supplied to the single-phase EMUs rectifier is not less than the increased energy in single-phase EMUs rectifier over a given period of time. Therefore, the single-phase EMUs rectifier system is strictly passive. If a system is strictly passive, according to system requirements and appropriate storage functions, a passive control law can be designed. Thus, it is possible to design a passive controller of the rectifier.

The LFO causes fluctuations in the voltage and current, and affects the energy distribution. To solve this problem, the method proposed in this paper studies the control of the single-phase EMUs rectifier from the energy variables of the system, and thus the method is feasible.

III. Control Law of the Single-Phase EMUs Rectifier Based on the IDA-PBC

A. Stable Equilibrium Point of the Single-Phase EMUs Rectifier System

The key aspect of IDA-PBC is that the new energy function can be minimized at the equilibrium point of the system using damping injection, and thus, the stable equilibrium point of the single-phase EMUs rectifier system should first be calculated. To obtain the equilibrium point, the control objectives for the single-phase EMUs rectifier are listed below.

1) The DC value $\langle q(t)\rangle_0/C$ of the output voltage $u_d = q(t)/C$ should be equal to a desired constant value that satisfies $U_d > U_{im}$.
2) The power factor of the converter should be equal to 1. This means that, in the steady state, the inductor current follows a sinusoidal signal with the same frequency and phase as the line voltage.

The desired stable equilibrium point of the system is obtained from the steady-state analysis of the single-phase EMUs rectifier state space model in [19].

$$\begin{aligned}x^* &= \left[x_1^*\ x_2^*\ x_3^*\right] \\ &= \left[\frac{1}{2}C^2U_d^2, 0, \frac{-\frac{U_{im}L_i}{2R_i} + \sqrt{\left(\frac{U_{im}L_i}{2R_i}\right)^2 - \frac{2U_d^2L_i^2}{R_iR_1}}}{2}\right]^T\end{aligned} \tag{15}$$

B. The Control Law of the Single-Phase EMUs Rectifier Based on IDA-PBC

Based on the IDA-PBC control principle, the control objective is to assign a desired energy function to the closed-loop of the single-phase EMUs rectifier by configuring the interconnection matrix and inserting the damping dissipation term. The desired target dynamics is a Hamiltonian system with the form

$$\dot{\boldsymbol{x}} = (\boldsymbol{J}_d - \boldsymbol{R}_d)(\nabla H_d)^T \tag{16}$$

where $\boldsymbol{J}_d = -\boldsymbol{J}_d^T$ and $\boldsymbol{R}_d = \boldsymbol{R}_d^T \geq 0$. $\boldsymbol{J}_d$ and $\boldsymbol{R}_d$ are new targeted interconnection and damping matrices, respectively. The new energy function $H_d(\boldsymbol{x})$ has a strict local minimum at the desired equilibrium $\boldsymbol{x}^*$.

To minimize $H_d(\boldsymbol{x})$ at the desired equilibrium point, the following equation should be satisfied

$$(\boldsymbol{J} - \boldsymbol{R})(\nabla H)^T + \boldsymbol{g} = (\boldsymbol{J}_d - \boldsymbol{R}_d)(\nabla H_d)^T \tag{17}$$

where $H_d(\boldsymbol{x}) = H(\boldsymbol{x}) + H_a(\boldsymbol{x})$,$\boldsymbol{J}_d = \boldsymbol{J} + \boldsymbol{J}_a$, $\boldsymbol{R}_d = \boldsymbol{R} + \boldsymbol{R}_a$ and $\boldsymbol{g} = \boldsymbol{g}_1(x_1)i_d + \boldsymbol{g}_2U_{im}$.

Let $\boldsymbol{J}_a = \boldsymbol{R}_a = 0$. Then, $\boldsymbol{J}_d = \boldsymbol{J}$ and $\boldsymbol{R}_d = \boldsymbol{R}$. Equation (17) can be simplified to

$$-(\boldsymbol{J} - \boldsymbol{R})(\nabla H_a)^T + \boldsymbol{g} = 0 \tag{18}$$

Defining $\boldsymbol{k}(\boldsymbol{x}) = (k_1, k_2, k_3)^T = (\nabla H_a)^T$, it follows that

$$\begin{cases} u_1 = \dfrac{R_ik_2 - \omega_sL_ik_3}{2k_1} \\ u_2 = \dfrac{\omega_sL_ik_2 + R_ik_3 - U_{im}}{2k_1} \\ R_i(k_2^2 + k_3^2) - U_{im}k_3 - 2i_d\sqrt{2x_1}k_1 = 0 \end{cases} \tag{19}$$

According to the configuration conditions of the desired equilibrium point, $K(x)$ satisfies $K(\boldsymbol{x}^*) = -\frac{\partial H(\boldsymbol{x}^*)}{\partial \boldsymbol{x}}$ at the desired

equilibrium point $\boldsymbol{x}^*$.

$$\begin{cases} k_1(x_1^*) = -\dfrac{1}{C}\sqrt{\dfrac{x_1^*}{x_1}} \\ k_1(x_2^*) = -\dfrac{2}{L_i}x_2^* \\ k_1(x_3^*) = -\dfrac{2}{L_i}x_3^* \end{cases} \tag{20}$$

Combining the above conditions, it can be derived that

$$H_a = -\frac{2\sqrt{x_1^*}}{C}\sqrt{x_1} - \frac{2}{L_i}x_3^* x_3 \tag{21}$$

Thus,

$$H_d = \frac{1}{C}x_1 + \frac{1}{L_i}x_2^2 + \frac{1}{L_i}x_3^2 - \frac{2\sqrt{x_1^*}}{C}\sqrt{x_1} - \frac{2}{L_i}x_3^* x_3 \tag{22}$$

From the storage function $H_d(\boldsymbol{x})$ of the closed-loop system in (22), it can be determined that

$$\begin{aligned} \frac{dH_d(\boldsymbol{x})}{dt} &= \left(\frac{\partial H_d(\boldsymbol{x})}{\partial \boldsymbol{x}}\right)\dot{\boldsymbol{x}} = \left(\frac{\partial H_d(\boldsymbol{x})}{\partial \boldsymbol{x}}\right) \\ &\quad \times \left[(\boldsymbol{J}_d - \boldsymbol{R}_d)(\nabla H_d)^T\right] \\ &= -\frac{\partial H_d(\boldsymbol{x})}{\partial \boldsymbol{x}}(\boldsymbol{R} + \boldsymbol{R}_a)\left(\frac{\partial H_d(\boldsymbol{x})}{\partial \boldsymbol{x}}\right)^T \end{aligned} \tag{23}$$

The effect of the newly inserted damping dissipation term $\boldsymbol{R}_a$ is to accelerate the energy dissipation of the single-phase EMUs rectifier [20]. It can be seen from (23) that the larger $\boldsymbol{R}_a$ is, the faster the system converges to the desired equilibrium point. Thus, the adjustment time of the single-phase EMUs rectifier is shortened.

From the above description, the control law can be expressed as

$$u_1 = -\frac{2\omega_s C x_3^* u_d}{U_d} \tag{24}$$

$$u_2 = -\frac{CL_i i_d u_d}{2x_3^*} \tag{25}$$

Combining (5) and the GSSA inverse transformation, it can be derived that

$$\upsilon = 2(u_1 \cos(\omega_s t) - u_2 \sin(\omega_s t)) \tag{26}$$

The passive control law of the single-phase EMUs rectifier is

$$S_d = \frac{2\omega_s x_3^*}{U_d}\cos(\omega_s t) - \frac{L_i i_d}{x_3^*}\sin(\omega_s t) \tag{27}$$

According to the IDA-PBC control law in (27), the control schematic diagram of IDA-PBC control of the single-phase EMUs rectifier is shown in Fig. 3.

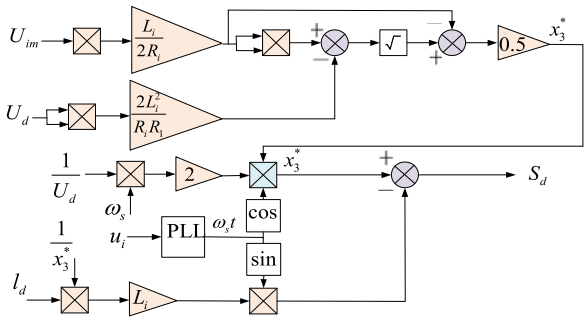

Fig. 3. Control schematic diagram of IDA-PBC control for the single-phase EMUs rectifier.

C. The Stability Analysis of the Single-Phase Rectifier

Let the state variable $\boldsymbol{x}$ of the single-phase EMUs rectifier be equal to the desired equilibrium point $\boldsymbol{x}^* = [x_1^*, \quad 0, \quad x_3^*]^T$ in (15), and $K(\boldsymbol{x}^*) = -\frac{\partial H(\boldsymbol{x}^*)}{\partial \boldsymbol{x}}$. Combining (20), it follows that

$$\frac{\partial k(\boldsymbol{x}^*)}{\partial \boldsymbol{x}} = 0 \tag{28}$$

From (22), the Hessian matrix of H_d can be obtained

$$\left.\frac{\partial^2 H_d}{\partial \boldsymbol{x}^2}\right|_{\boldsymbol{x}=\boldsymbol{x}^*} = \begin{pmatrix} \dfrac{1}{2C\sqrt{x_1^*}} & 0 & 0 \\ 0 & \dfrac{2}{L_i} & 0 \\ 0 & 0 & \dfrac{2}{L_i} \end{pmatrix} \tag{29}$$

Through the analysis of (29), it can be determined that the Hessian matrix of H_d satisfies the requirement that it is greater than zero. From (28) and (29), it can be seen that

$$\frac{\partial k(\boldsymbol{x}^*)}{\partial \boldsymbol{x}} > -\left.\frac{\partial^2 H_d}{\partial \boldsymbol{x}^2}\right|_{\boldsymbol{x}=\boldsymbol{x}^*} \tag{30}$$

Combining (30) and the Lyapunov stability theory, it can be seen that the closed-loop controlled-dissipative Hamiltonian system of the single-phase EMUs rectifier is stable at the desired equilibrium point $\boldsymbol{x}^* = [x_1^*, \quad 0, \quad x_3^*]^T$ in [21].

From (22), it can be derived that

$$\begin{aligned} &\frac{\partial H_d(\boldsymbol{x})}{\partial \boldsymbol{x}}\boldsymbol{R}_d\left(\frac{\partial H_d(\boldsymbol{x})}{\partial \boldsymbol{x}}\right)^T \\ &= \begin{bmatrix} 0 & 0 & 0 \\ 0 & \dfrac{R_i}{2}\left(\dfrac{2x_2}{L_i}\right)^2 & 0 \\ 0 & 0 & \dfrac{R_i}{2}\left(\dfrac{2x_3}{L_i} - \dfrac{2}{L_i}x_3^*\right)^2 \end{bmatrix} \end{aligned} \tag{31}$$

When $\boldsymbol{x} = \boldsymbol{x}^*$, (31) can have a minimum value of zero. According to the LaSalle invariant set theorem and its conditions, $\boldsymbol{x}^*$ is the isolated minimum of energy function $H_d(x)$ of the single-phase EMUs rectifier, and the largest invariant set of the closed-loop system in the range of (32) is equal to $\{\boldsymbol{x}^*\}$, thus it is proved that the single-phase EMUs rectifier is asymptotically

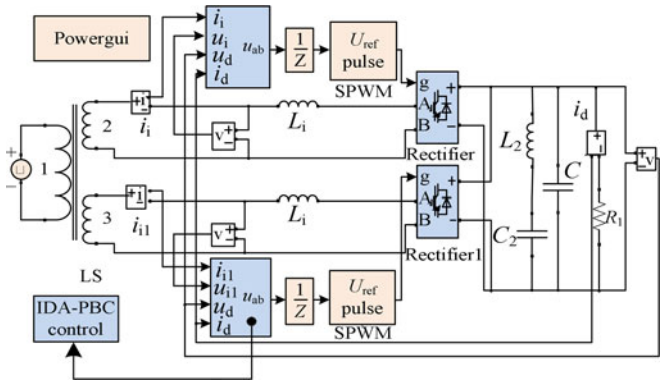

Fig. 4. Simulation model of double four-quadrant pulse rectifiers.

TABLE I
PARAMETERS OF THE RECTIFIER MODEL

Parameters	Value	Parameters	Value
Input voltage u_i(V)	1550	$R_1(\Omega)$	10
Input current i_i(A)	460	U_d(kV)	3.0
C(mF)	1	C_2(mF)	3
L_i(mH)	5	L_2(mH)	0.84

stable under the passive control.

$$\left\{ \boldsymbol{x} \in R^n \left| \left(\frac{\partial H_d(\boldsymbol{x})}{\partial \boldsymbol{x}} \right)^T \boldsymbol{R}_d(\boldsymbol{x}) \frac{\partial H_d(\boldsymbol{x})}{\partial \boldsymbol{x}} = 0 \right. \right\} \tag{32}$$

IV. Simulation Modeling and Verification

To further verify the superiority of the proposed control scheme, the PBC is compared with the traditional PI, ADRC and MC. The simulations of the model based on these controllers applied to the single-phase EMUs rectifier are carried out in Matlab/Simulink and RT-LAB, and the simulations of EMUs in the traction network based on PBC are carried out to further verify the suppression of the LFO.

A. Offline Simulation of Double-Four Quadrant Rectifiers

An offline simulation model of double-four quadrant EMUs rectifiers is built in MATLAB/Simulink, as shown in Fig. 4. The parameters are listed in Table I, and the switching frequency of the IGBT is 350 Hz and a bipolar carrier PWM algorithm is adopted in the PWM. Based on the PI, MC, ADRC and PBC controllers, the line voltage and line current waveforms are depicted in Fig. 5(a), Fig. 5(b), Fig. 5(c) and Fig. 5(d), respectively. The voltage waveforms of the DC-link output of the double-four quadrant EMUs rectifier adopting the PI, MC, ADRC and PBC controllers are shown in Fig. 6. The performance indexes of the DC-link voltage are listed in Table II. In Fig. 5(a), the line current increases up to 0.1 s, then tends to be stable after about 0.25 s. In Fig. 5(b), the line current is small at the beginning, and then suddenly increases at 0.1 s. And the line current reaches a steady state after about 0.35 s. In Fig. 5(c) and Fig. 5(d), the line current is large at starting and then decreases. And the stable duration of the line current in Fig. 5(c) and Fig. 5(d) is nine

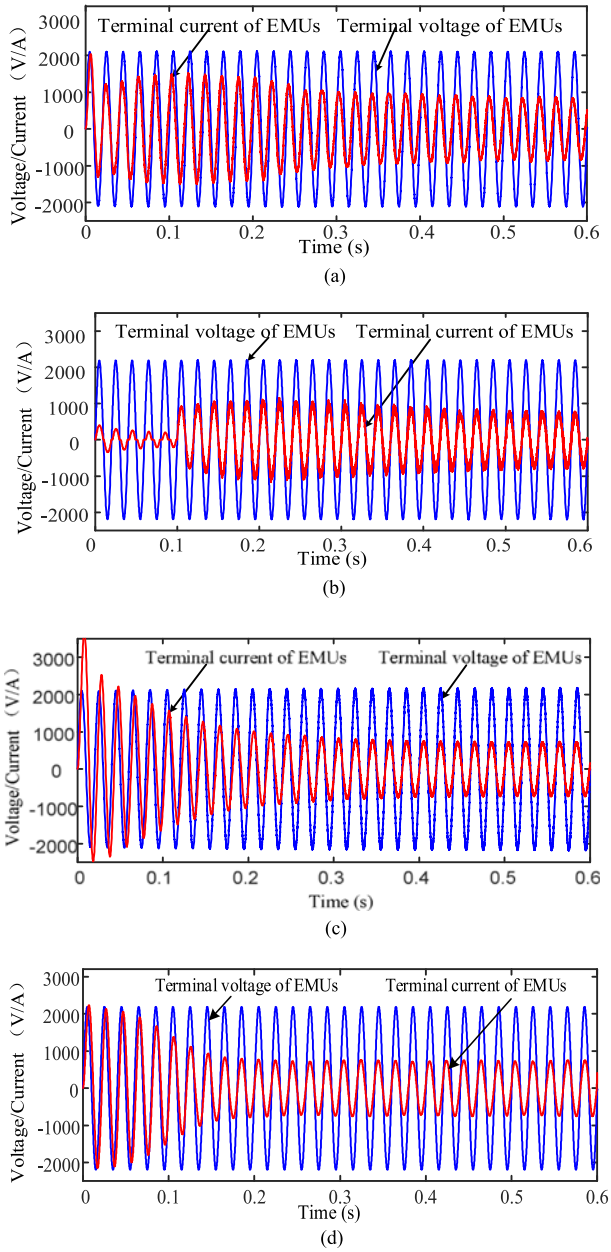

Fig. 5. AC voltage and current waveforms. (a) AC voltage and current with PI; (b) AC voltage and current with MC; (c) AC voltage and current with ADRC; (d) AC voltage and current with IDA-PBC.

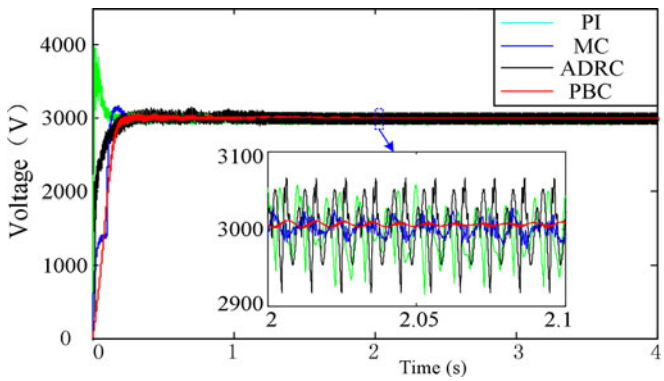

Fig. 6. DC-link voltage of EMUs rectifier in rated load.

TABLE II
DC-LINK VOLTAGE PERFORMANCE INDEXES OF DOUBLE RECTIFIERS

Performance	PI control	MC	ADRC	PBC
Overshoot (%)	32.4	5.5	Very little	Very little
Peak time (s)	0.013	0.182	None	None
Adjustment time (s)	0.24	0.33	0.18	0.22
Voltage fluctuation(V)	±70	±23	±60	±8

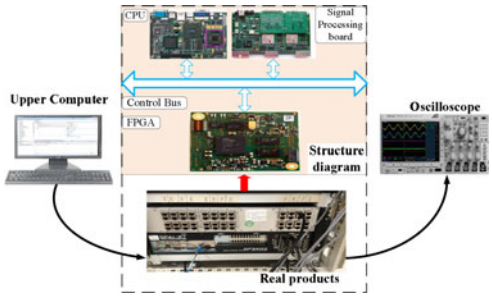

Fig. 7. Structure of the real-time experimental platform.

and eight periods, respectively. Analysis of Fig. 5(a), (d) by the fast Fourier transform (FFT) method indicates that the line current total harmonic distortion (THD) of the EMUs rectifier based on the PI controller, MC controller and ADRC controller, are 27.52%, 28.62% and 21.32%, respectively. The line current THD of the EMUs rectifier based on the PBC controller is significantly reduced to 3.98%, and the power factor is closer to unity.

As illustrated in Fig. 6 and Table II, the above four controllers can achieve the expected control. The voltage fluctuation range of the PBC controller is only ±8 V, which is significantly better than the ADRC and PI controllers. The voltage overshoot is almost zero for the PBC controller, while the PI controller overshoot of 32.4% is much larger. In Table II, the adjustment time of the PBC controller is decreased by 33% compared to that of the MC controller. Fig. 6 and Table II show that the peak time of the PBC controller is much less than that of the MC controller. Thus, the PBC controller has better static performance and dynamic performance.

B. Real-Time Simulation of Double-Four Quadrant EMUs Rectifiers

To further validate the performance of the proposed method, some real-time online simulations are implemented by using a real-time experimental platform, which consists of a real-time RT-LAB OP5600 simulator, an upper computer and an oscilloscope. The structural diagram of the real-time online simulation system is shown in Fig. 7. The parameter values are the same as those of the offline simulation.

The line and DC-link voltage and current waveforms of the EMUs rectifier based on the PBC controller as displayed by the oscilloscope in the real-time experimental platform are shown in Fig. 8(a). The waveforms obtained from the experimental data are shown in Fig. 8(b). The experimental data are from the real-time experiment that matches the waveforms in Fig. 8(a).

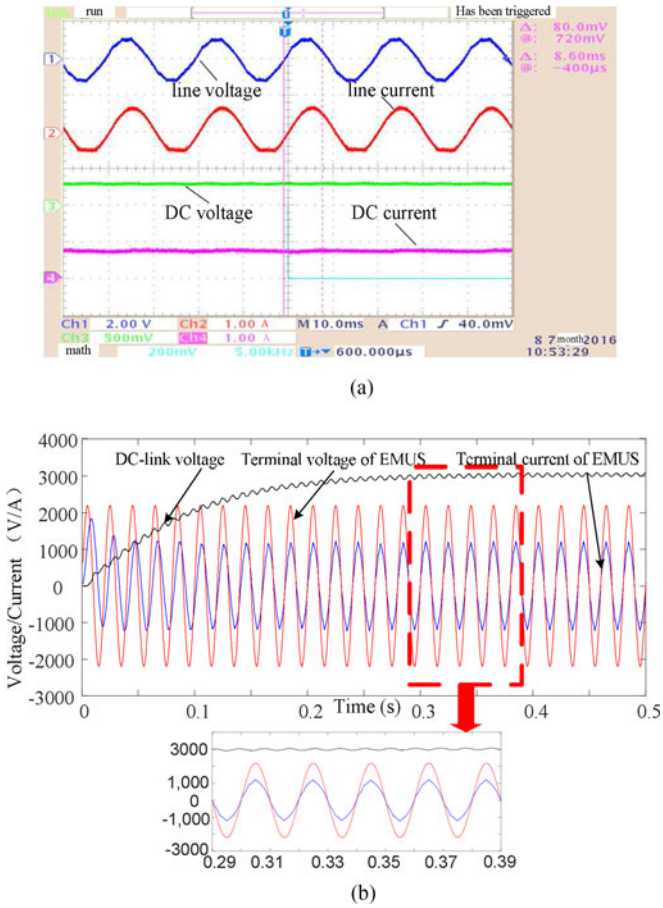

Fig. 8. Line and DC-link voltage and current waveforms. (a) The waveforms displayed by the oscilloscope; (b) The waveforms from the experimental data.

Fig. 8(a) shows that the distortion rates of the line voltage and current represented by CH1 and CH2 are low, and the power factor is closer to unity. The fluctuations of the DC-link voltage and current represented by CH3 and CH4 are small. In Fig. 8(b), the line current THD is 13.23%, and the voltage adjustment time and voltage fluctuation are 0.2 s and ±45 V, respectively. In addition, the voltage overshoot is very small. Therefore, these results further validate the performance of the PBC controller.

C. Simulations of Multi-EMUs in a Traction Network Based on PI and PBC Controllers

To test the feasibility of the proposed PBC strategy in systems of greater complexity and to verify the suppression effect on the LFO, the reduced order model of the traction network is built as shown in Fig. 9 [22]. From the uplink traction substation in the traction network, n EMUs are assessed at the position between T and N at a distance of 10 km, and the electrical characteristics of the ETNECS can be further studied.

When EMUs based on the PI controller are assessed in the reduced order model of the traction network, the system can be stable if the number of EMUs is less than 6. However, the system is unstable if the number of EMUs reaches 6 or more. The waveforms of the traction network voltage, current and DC-link voltage for an input of 6 EMUs are shown in Fig. 10.

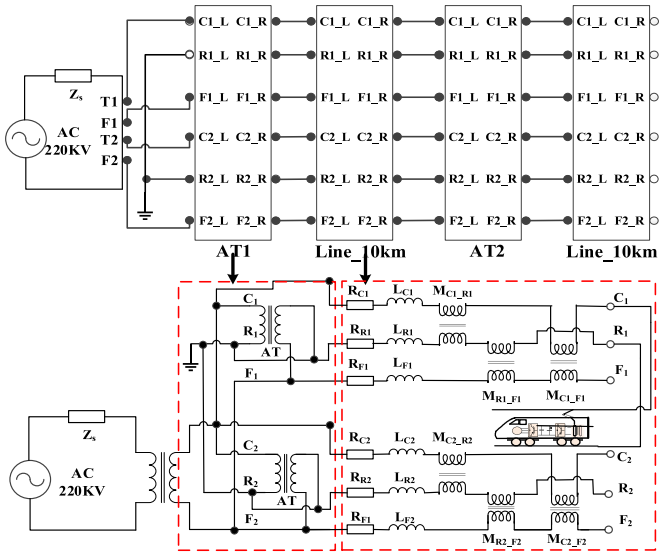

Fig. 9. Simulation model of an EMUs-traction network cascade system.

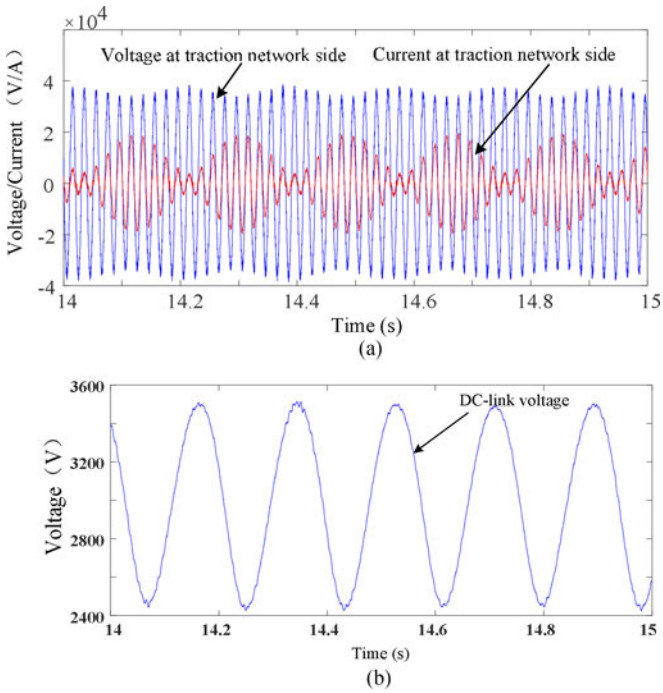

Fig. 10. Voltage and current waveforms of the 6 EMUs input based on the PI controller. (a) Voltage and current waveforms on the traction network side; (b) DC-link voltage waveforms.

To facilitate observation of the voltage LFO phenomenon, the traction network current is amplified 100 times and is shown with the traction network voltage in Fig. 10(a).

As illustrated in Fig. 10(a), the low-frequency modulation signal occurs in the traction network voltage and current, and the voltage peak fluctuates between 33 kV and 39 kV. The oscillation frequency is approximately 5.6 Hz. In Fig. 10(b), the range of the DC-link voltage amplitude fluctuation is from 2400 V to 3600 V. Obviously, the momentary fluctuation of electric quantities indicates that an increase in the number of EMUs will lead to an increase of the line voltage and current

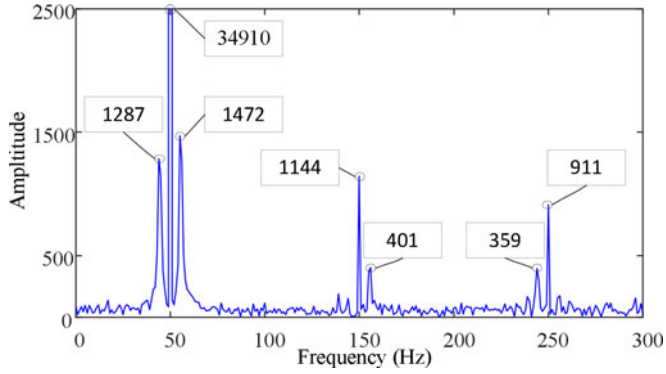

Fig. 11. FFT spectrum analysis of the traction network side voltage.

TABLE III
MODAL ANALYSIS OF OSCILLATION SIGNAL FROM PI CONTROLLER WITH ESPRIT

Attenuation coefficient	Frequency/ Hz	Amplitude/V	Phase/°
−0.0197	50	34792	68
0.0706	55	2077	77
0.0971	45	1852	−176
0.1725	150	957	57
0.3018	250	664	−5
−0.4227	850	552	−11
−0.1816	155	473	89

fluctuations and a decrease of the PI regulator dynamic tracking performance.

To precisely analyze the modes of the oscillation signal, the FFT analysis and estimating signal parameters via rotational invariance techniques (ESPRIT) are adopted to estimate the frequency of the LFO. The results of the FFT frequency estimation for the traction side voltage signal are shown in Fig. 11, and Table III gives the results from the ESPRIT analysis with the modal order 7.

In Fig. 11 and Table III, there are components at 55 Hz, 45 Hz, 150 Hz, 155 Hz, 250 Hz and other frequencies outside the fundamental frequency component in the FFT and ESPRIT modal analysis results. Based on the FFT transform, the voltage signal obviously has high frequency interference, which generates additional frequency components. The ESPRIT modal analysis clearly overcomes this defect. Fig. 11 shows that there is a component at 245 Hz, which is not found in Table III. According to the modal analysis results, and referring to IEC 61000-4-15-1997 and GB12326-2008, when the load on the power grid drastically changes and the impact load is switched, the relevant electrical amplitude will intermittently fluctuate in the 0.9–1.1 pu range and symmetrical frequency components of 0.05–35 Hz appear near the main frequency. There is a clear agreement between the dominant mode of the EMUs-traction network system voltage instability phenomenon and this provision. It can be seen that the attenuation coefficient reflects the main frequency in Table III. For example, the attenuation coefficient of the most important frequency component, namely, the fundamental frequency, is the smallest. When there are 6 multi-EMUs based on the proposed PBC control strategy in the

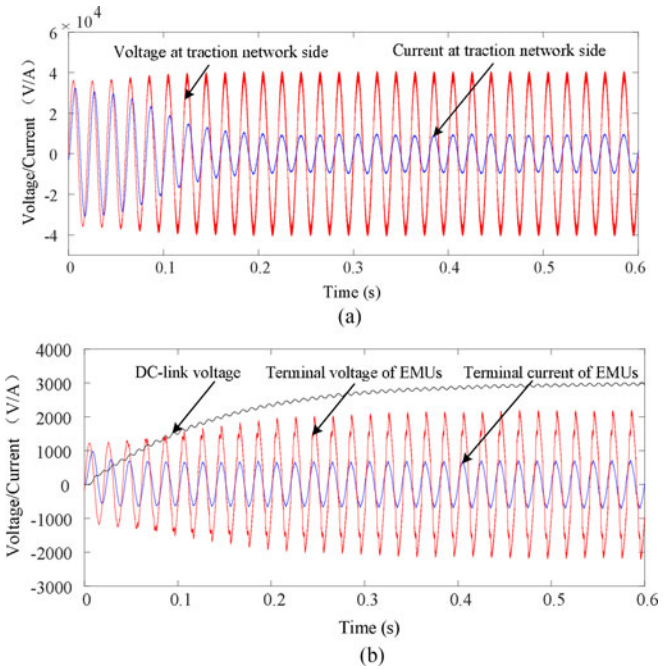

Fig. 12. Voltage and current waveforms for an input of 6 EMUs based on PBC. (a) Voltage and current waveforms of the traction network side; (b) Voltage and current waveforms of the EMUs.

TABLE IV
MODAL ANALYSIS OF THE OSCILLATION SIGNAL FROM PBC WITH ESPRIT

Attenuation coefficient	Frequency/Hz	Amplitude/V	Phase/°
0.0031	50	38664	−100
0.0523	950	1468	−63
0.0125	850	538	−10
−0.2691	150	243	−172
0.1342	250	161	137
−0.3278	750	67	51
−0.4592	650	52	100

traction network, the ETNECS operation is stable. As the number of EMUs continues to increase, the system remains stable. The voltage and current waveforms for the case of 6 EMUs are shown in Fig. 12. The traction network current has been amplified 100 times, as before, and is shown with the traction network voltage in Fig. 12(a). In Fig. 12(a), the current is large at starting and then decreases, and stabilizes at about 0.2 s. The traction network voltage and current are stable at 40 kV and 100 A, respectively, and the current THD is 2.14%. In Fig. 12(b), the DC-link voltage increases from 0 V to 3000 V in 0.3 s. The DC-link voltage is stable at 2970 V, and the voltage fluctuation is ±40 V. The line voltage increases at the beginning and reaches a steady state at about 0.2 s, and the current THD is 4.85%. The line voltage is stable at 2190 V. Thus, the PBC proposed in this paper significantly suppresses the voltage LFO.

The results of the analysis of the traction side voltage signal based on PBC using the ESPRIT method with the modal order 7 are shown in Table IV. Analysis and comparison with Tables III and IV reveal that the energies of the symmetrical frequency components are greatly reduced, e.g., the energies at 45 Hz and 55 Hz. The frequency components at 45 Hz, 55 Hz and 155 Hz no longer exist in the case of PBC, and the energy of the fundamental frequency component increases. In addition, the energies of the frequency components at 150 Hz and 250 Hz are reduced by 74.6% and 75.8%, respectively. Compared with the PI controller, the PBC has a better effect on the single-phase EMUs rectifier.

V. CONCLUSIONS

The application of traditional PI controller is one of most important factors causing the voltage LFO of the high-speed railway traction network. In this paper, based on the characteristics of the nonlinearity of the single-phase EMUs rectifier, a nonlinear controller with PBC is designed to optimize the load characteristics of the single-phase EMUs rectifier. The single-phase EMUs rectifier based on the PBC has been analyzed and modeled. The LFO signal modal analysis is implemented and simulations are carried out. Some conclusions can be drawn: (1) For the control of the single-phase EMUs rectifier, the PBC controller has better dynamic performance and static performance than the PI, MC and ADRC controllers, and it can effectively suppress the voltage LFO of the high-speed railway traction network. (2) The PBC controller can suppress the symmetrical frequency components and effectively reduce the 3rd, 5th and other harmonic components. (3) The FFT analysis and ESPRIT modal analysis are adopted to realize the modal analysis of the LFO. The ESPRIT algorithm can overcome the disadvantage of FFT analysis and is suitable to extract the oscillation frequency of the LFO.

REFERENCES

[1] Y. Liao, Z. Liu, G. Zhang, and C. Xiang, "Vehicle-grid system modeling and stability analysis with forbidden region based criterion," *IEEE Trans. Power Electron.*, vol. 32, no. 5, pp. 3499–3512, May 2017.
[2] E. Mollerstedt and B. Bernhardsson, "Out of control because of harmonics-an analysis of the harmonic response of an inverter locomotive," *IEEE Control Syst.*, vol. 20, no. 4, pp. 70–81, Aug. 2000.
[3] L. Li, C. Liu, and H. Ben, "Research of the dynamic characteristics of the PWM converter based on neurons PI control," *Power Syst. Protection Control*, vol. 41, no. 11, pp. 124–128, 2013.
[4] H. Wang and M. Wu, "Analysis of low-frequency oscillation in electric railways based on small-signal modeling of vehicle-grid system in dq frame," *IEEE Trans. Power Electron.*, vol. 30, no. 9, pp. 5318–5330, Sep. 2015.
[5] S. Menth and M. Meyer, "Low frequency power oscillations in electric railway systems," *Elektrische Bahnen*, vol. 104, no. 5, pp. 216–221, 2006.
[6] Z. Han, L. Tang, and W. Li, "Causal analysis and resolution of the voltage instability between AC drive electric locomotive and power supply network," *J. China Railw. Soc.*, vol. 33, no. 10, pp. 25–28, 2011.
[7] Z. Liu, G. Zhang, and Y. Liao, "Stability research of high-speed railway EMUs and traction network cascade system considering impedance matching," *IEEE Trans. Ind. Appl.*, vol. 52, no. 5, pp. 4315–4326, Sep./Oct. 2016.
[8] C. Heising, M. Oettmeier, V. Staudt, A. Steimel, and S. Danielsen, "Improvement of low-frequency railway power system stability using an advanced multivariable control concept," in *Proc. IEEE 35th Annu. Conf. Ind. Electron.*, 2009, pp. 560–565.
[9] X. Feng, *Electric Traction AC Drives and Control System*. Beijing, China: Higher Educ. Press, 2009.
[10] G. Zhang, Z. Liu, S. Yao, Y. Liao, and C. Xiang, "Suppression of low-frequency oscillation in traction network of high-speed railway based on auto-disturbance rejection control," *IEEE Trans. Transp. Electrific.*, vol. 2, no. 2, pp. 244–255, Jun. 2016.

[11] R. Zhao *et al.*, "Design of decentralized controllers for parallel AC-DC system based on effective relative gain array and mixed H2/H∞ control," *Power Syst. Protection Control*, vol. 44, no. 24, pp. 44–51, 2016.
[12] Q. Zhang and G. Liu, "Precise control of elastic joint robot using an interconnection and damping assignment passivity-based approach," *IEEE/ASME Trans. Mechatronics*, vol. 21, no. 6, pp. 2728–2736, Dec. 2016.
[13] D. D. Puerto-Flores, J. M. A. Scherpen, M. Liserre, M. M. J. de Vries, M. J. Kransse, and V. G. Monopoli, "Passivity-based control by series/parallel damping of single-phase PWM voltage source converter," *IEEE Trans. Control Syst. Technol.*, vol. 22, no. 4, pp. 1310–1322, Jul. 2014.
[14] T. L. Vu and K. Turitsyn, "Lyapunov functions family approach to transient stability assessment," *IEEE Trans. Power Syst.*, vol. 31, no. 2, pp. 1269–1277, Mar. 2016.
[15] M. R. Mojallizadeh and M. A. Badamchizadeh, "Adaptive passivity-based control of a photovoltaic/battery hybrid power source via algebraic parameter identification," *IEEE J. Photovolt.*, vol. 6, no. 2, pp. 532–539, Mar. 2016.
[16] Y. H. Gui, W. Kim, and C. C. Chung, "Passivity-based control with nonlinear damping for type 2 STATCOM systems," *IEEE Trans. Power Syst.*, vol. 31, no. 4, pp. 2824–2833, Jul. 2016.
[17] J. M. Scherpen, D. Jeltsema, and J. Klaassens, "Lagrangian modeling of switching electrical networks," *Syst. Control Lett.*, vol. 48, no. 5, pp. 365–374, 2003.
[18] R. Ortega *et al.*, "Interconnection and damping assignment passivity-based control of port-controlled Hamiltonian systems," *Automatica*, vol. 38, no. 4, pp. 585–596, 2002.
[19] C. Gaviria, E. Fossas, and R. Griñó, "Robust controller for a full-bridge rectifier using the IDA approach and GSSA modeling," *IEEE Trans. Circuits Syst. I; Reg. Papers*, vol. 52, no. 3, pp. 609–616, Mar. 2005.
[20] A. Donaire and S. Junco, "Energy shaping, interconnection and damping assignment, and integral control in the bond graph domain," *Simul. Modell. Pract. Theory*, vol. 17, no. 1, pp. 152–174, 2009.
[21] J. Wang, *Nonlinear Control of Voltage Source PWM Rectifier*. Beijing, China: China Mach. Press, 2008.
[22] H. Lee, C. Lee, G. Jang, and S.-h. Kwon, "Harmonic analysis of the Korean high-speed railway using the eight-port representation model," *IEEE Trans. Power Del.*, vol. 21, no. 2, pp. 979–986, Apr. 2006.

Zhigang Liu (M'06–SM'16) received the Ph.D. degree in power system and its automation from Southwest Jiaotong University, Chengdu, China, in 2003. He is currently a Full Professor at the School of Electrical Engineering, Southwest Jiaotong University, China. His research interests are the electrical relationship of EMUs and traction, catenary, and pantograph assessment of high-speed railway. He is an IET Fellow.

Zhaozhao Geng is currently working toward the Master's degree at the School of Electrical Engineering, Southwest Jiaotong University, Chengdu, China. Her research interest is the traction power system stability enhancement with multi-EMUs accessed.

Xinxuan Hu is currently working toward the Master's degree at the School of Electrical Engineering, Southwest Jiaotong University, Chengdu, China. His research interest is the traction power system stability enhancement with multi-EMUs accessed.